

The younger flagellum coordinates the beating in *C. reinhardtii*

Da Wei^{1,3}, Greta Quaranta², Marie-Eve Aubin-Tam^{1†}, Daniel S.W. Tam^{2*}

¹Department of Bionanoscience, Delft University of Technology,
2628CJ Delft, Netherlands.

²Laboratory for Aero and Hydrodynamics, Delft University of Technology,
2628CD Delft, Netherlands.

³Beijing National Laboratory for Condensed Matter Physics, Institute of Physics,
Chinese Academy of Sciences; Beijing 100190, China.

†Corresponding author. Email: m.e.aubin-tam@tudelft.nl;

*Corresponding author. Email: d.s.w.tam@tudelft.nl.

Abstract

Eukaryotes swim with coordinated flagellar (ciliary) beating and steer by fine-tuning the coordination. The model organism for studying flagellate motility, *C. reinhardtii* (CR), employs synchronous, breast-stroke-like flagellar beating to swim, and it modulates the beating amplitudes differentially to steer. This strategy hinges on both inherent flagellar asymmetries (e.g. different response to chemical messengers) and such asymmetries being effectively coordinated in the synchronous beating. In CR, the synchrony of beating is known to be supported by a mechanical connection between flagella, however, how flagellar asymmetries persist in the synchrony remains elusive. For example, it has been speculated for decades that one flagellum leads the beating, as its dynamic properties (i.e. frequency, waveform, etc.) appear to be copied by the other one. In this study, we combine experiments, computations, and modeling efforts to elucidate the roles played by each flagellum in synchronous beating. With a non-invasive technique to selectively load each flagellum, we show that the coordinated beating essentially responds to only load exerted on the *cis* flagellum; and that such asymmetry in response derives from a unilateral coupling between the two flagella. Our results highlight a distinct role for each flagellum in coordination and have implication for biflagellates' tactic behaviors.

One-Sentence Summary: The younger flagellum of *C. reinhardtii* coordinates the synchronous beating and couples to external forces.

Introduction

The ability to swim towards desirable environments and away from hazardous ones is fundamental to the survival of many microorganisms. These so-called tactic behaviors are exhibited by many motile microorganisms ranging from bacteria (1, 2) to larger flagellates and ciliates (3–5). Different microorganisms have developed specific strategies for steering, depending on the tactic behavior and on their specific sensory and motility repertoire. For example, bacteria modulate the tumbling rate (1) while flagellates and ciliates modulate the waveform (6–9), amplitude (10, 11) and frequency of their flagellar/ciliary (4, 12) beating. The goal of these active modulations of the motility is to achieve a spatially asymmetric generation of propulsive force to steer the organism.

C. reinhardtii (CR), the model organism for studies of flagellar motility, achieves tactic navigation by a fine-tuned differential modulation on its two flagella. Studying this organism offers great opportunities to look into how flagella coordinate with each other and how such coordination helps facilitate targeted steering. CR has a symmetric cell body and two near-identical flagella inherited from the common ancestors of land plants and animals (13). It swims by beating its two flagella synchronously and is capable of photo- and chemotaxis (10, 14). For this biflagellated organism, effective steering hinges on both flagellar asymmetry and flagellar coordination. On the one hand, the two flagella must be asymmetric to respond differentially to stimuli (10, 15); on the other hand, the differential responses must be coordinated by the cell such that the beating would remain synchronized to guarantee effective swimming. Understanding this remarkable feat requires knowledge about both flagellar asymmetry and coordination.

The two flagella are known to be asymmetric in several, possibly associated, aspects. First of all, they differ in developmental age (16, 17). The flagellum closer to the eyespot, the *cis*(-eyespot) flagellum, is always younger than the other one, the *trans*(-eyespot) flagellum. This is because the *cis* is organized by a basal body (BB) that develops from a pre-matured one in the mother cell; and this younger BB also organizes the flagellar root (D4 rootlet) that dictates the eyespot formation (18). Second, the two flagella have asymmetric protein composition (19–21). For example, the *trans* flagellum is richer in CAH6, a protein possibly involved in CO₂ sensing (14, 20). Finally, the flagella have different dynamic properties (22–24). Their beating is modulated differentially by second messengers such as calcium (22, 23) and cAMP (25). When beating alone, the *trans* beats at a frequency 30%-40% higher than the *cis* (23, 26–28); the *trans* also displays an attenuated waveform (29) and a much stronger noise (29, 30).

Remarkably, despite these inherent asymmetries, CR cells establish robust synchronization between the flagella. Such coordination enables efficient swimming and steering of the cells and takes basis on the fibrous connections between flagellar bases (31, 32). Intriguingly, in the coordinated beating, both flagella display dynamic properties, i.e., flagellar waveform, beating frequency (~ 50 Hz), and frequency fluctuation, that are more similar to those of the *cis* flagellum (26, 28–30, 33). This has led to a long-standing hypothesis that “the *cis* somehow tunes the *trans* flagellum” (26). This implies that the symmetric flagellar beating (“breast-stroke”) observed is the result of interactions between two flagella playing differential roles in coordination. How does the basal coupling make this possible? Recent theoretical efforts show that the basal coupling can give rise to different synchronization modes (34–36); and that flagellar dynamics, such as beating frequency, may simply emerge from the interplay between mechanics of basal coupling and bio-activity (36). Yet, most theoretical efforts examining flagellar synchronization have assumed two identical flagella, limiting the results’ implication for the realistic case. Moreover, little experiments directly probe the flagella’s differential roles during synchronous beating (37). Therefore, flagellar coordination in this model organism remains unclear. To clarify the picture experimentally, one needs to selectively force each flagellum, and characterize the dynamics of the flagellar response.

In this study, we address this challenge and devise a non-invasive approach to apply external forces selectively on the *cis*- or the *trans*-flagella. Oscillatory background flows are imposed along an angle with respect to the cell’s symmetry axis. Such flows result in controlled hydrodynamic forces, which are markedly different on the two flagella. With experiments, hydrodynamic computations, and modeling, we show definitively that the two flagella are unilaterally coupled, such that the younger flagellum (*cis*) coordinates the beating, whereas the elder one simply copies the dynamic properties of the younger. This also means that only external forces on the *cis* may mechanically fine-tune the coordination. We also study the effect of calcium in the *cis*’ leading role as calcium is deeply involved in flagellar asymmetry and hence phototactic steering. In addition, a well-known mutant that lacks flagellar dominance (*ptx1*) (23, 38) is examined. Results show that the coordinating role of *cis* does not need environmental free calcium, whereas it does require the genes lost in *ptx1*. Our results discern the differential roles of CR’s flagella, highlight an advanced function of the inter-flagellar mechanical coupling, and have implications for biflagellates’ tactic motility.

Experimental scheme for selective loading

We set out to establish a non-invasive experimental technique that exerts differential loads on the flagella of CR. Following the study by Quaranta et al. (31), we induce oscillatory background flows to exert hydrodynamic forcing to flagella of captured cells. With programmed oscillations of the piezoelectric stage, the amplitude, frequency, and direction of the background flows are all controlled, enabling selective loading.

To quantitatively estimate the selectivity of the flows along different angles (θ), we compute the flagellar loads under the flows along $\theta = -45^\circ$, 0° , and 45° , see Fig. 1A. Computations based on boundary element methods (BEM) and slender-body theory (SBT) give the real-time drag force \mathbf{F} on each flagellum and the power P exerted by the viscous forces on each flagellum. For given realistic flagellar shapes, we compare computed loads with and without external flows. From these we isolate the loads from the induced flows \mathbf{F}_{Flow} and P_{Flow} (*Methods*).

Loads on each flagellum under flows of $\theta = 0^\circ$, -45° , 45° are presented in Fig. 2. Upper panels display the magnitude of the drag force $F_{\text{Flow}} = |\mathbf{F}_{\text{Flow}}|$; while lower panels show viscous power P_{Flow} . Force magnitudes are scaled by $F_0 = 6\pi\mu RU_0 = 9.9$ pN; while the powers by $P_0 = F_0 U_0 = 1.1$ fW. F_0 is the Stokes drag on a typical free-swimming cell (radius $R = 5$ μm , speed $U_0 = 110$ $\mu\text{m/s}$, water viscosity $\mu = 0.95$ mPa·s).

Evidently, along $\theta = 0^\circ$, flows load the flagella equally (Fig. 2A). However, at $\theta = -45^\circ$, flows load the *cis* flagellum ~ 2 times larger than the *trans* (Fig. 2B, $F_{\text{Flow}}^c \approx 2F_{\text{Flow}}^t$); whereas flows at $\theta = 45^\circ$ do the opposite (Fig. 2C). The selectivity also manifests in (the absolute values of) P_{Flow} . We do notice that flows along $\theta = +45^\circ$ are able to synchronize the flagella with $P_{\text{Flow}} < 0$, meaning that the flagella are working against the flows, and this shall be discussed in later sections.

Hereon forward, we refer to θ_c -flows, flows for which $\theta = -45^\circ$ and the *cis*-flagellum is selectively loaded. Likewise, θ_t -flows denote flows on $\theta = +45^\circ$ that selectively load the *trans*. θ_a -flows denote the axial flow along $\theta = 0^\circ$. We next introduce how we quantify the flows' effective forcing strength (ε) on the cell.

Phase dynamics of flagellar beating is extracted from videography (31, 39, 40). Recordings are masked and thresholded to highlight the flagella (Fig. 1B-C). Then the mean pixel values over time within two sampling windows (Fig. 1D) are converted to observable-invariant flagellar phases (41), Fig. 1E. Throughout this study, as *cis* and *trans* always beat synchronously (Fig. 1E inset), their phases $\varphi_{c,t}$ are used interchangeably as the flagellar phase φ . The flagellar phase

dynamics under external periodic forcing is described by Adler equation (42–44):

$$\frac{d\Delta\varphi}{dt} = -2\pi\nu - 2\pi\varepsilon \sin(\Delta\varphi) + \zeta(t). \quad (1)$$

$\Delta\varphi = \varphi - 2\pi f_f t$ is the phase difference between the beating and the forcing, with f_f the forcing frequency, and ε the forcing strength. The detuning $\nu = f_f - f_0$ is the frequency mismatch between the beating (f_0) and forcing. $\zeta(t)$ represents a white noise that satisfies $\langle \zeta(\tau + t)\zeta(\tau) \rangle = 2T_{\text{eff}}\delta(t)$, with T_{eff} an effective temperature and $\delta(t)$ the Dirac delta function.

When the forcing strength outweighs the detuning ($\varepsilon > |\nu|$), synchronization with the flow ($d\Delta\varphi/dt = 0$) emerges, see the plateaus marked black in Fig. 1F. We characterize synchronization with $\tau = t_{\text{sync}}/t_{\text{tot}}$, where t_{sync} is the total time of flow synchronization and t_{tot} the flow duration. Fig. 1F presents the phase dynamics which are representative and range from: no synchronization ($\tau=0$, *i*), unstable synchronization ($0 < \tau < 1$, *ii-iii*), and stable synchronization ($\tau=1$, *iv*). In this study, the frequency range in ν for which $\tau \geq 0.5$ is used to measure ε (see Fig. 1F inset). This method is equivalent to previous fitting-based methods (28, 31), see **SM. Sec.S1**.

Asymmetric susceptibility to flow synchronization

Now we examine cell responses to flows of various amplitudes and along different directions. First we explore flow synchronization over a broad range of amplitudes and frequencies. θ_a -flows with frequencies $f_f \in [40, 75]$ Hz and amplitudes $U \in [390, 2340]$ $\mu\text{m/s}$ are imposed. The scanned range covers reported intrinsic frequencies of both the *cis* and *trans* flagellum (22, 24, 26, 27); while the amplitude reaches the maximum instantaneous speed of a beating flagellum (~ 2000 $\mu\text{m/s}$). Fig. 3A displays the resultant flow-synchronized time fractions τ . Up until the strongest flow amplitude, the large forces cannot disrupt the synchronized flagellar beating. In addition, synchronization is never established around frequencies other than f_0 . This shows that the inter-flagella coupling is much stronger than the maximum amplitude of forcing.

Next we examine the synchronization with the θ_c -flows and θ_t -flows. Flows of a fixed amplitude ($\sim 7U_0$) but varying frequencies around f_0 are applied to each captured cell (see *Methods*). With these, the flow-synchronized time fraction τ as a function of the detuning (ν) and flow direction ($\theta_{c,a,t}$) is recorded and helps quantify the flows' effective forcing $\varepsilon(\theta)$.

Comparing $\tau(\nu; \theta_c)$ to $\tau(\nu; \theta_t)$, with $\tau(\nu; \theta_a)$ as reference, we find that θ_c -flows are the most effective in synchronizing the beating (Fig. 3B). We illustrate this point with the profiles of an

exemplary cell (Fig. 3B inset). First, although both the θ_c -flow (red) and the θ_t -flow (blue) can synchronize the cell at small detunings ($|\nu| < 0.5\text{Hz}$), the θ_c -flow maintains the synchronization for the whole time ($\tau(\theta_c) = 1$), while the θ_t -flow for a slightly smaller time fraction ($\tau(\theta_t) \approx 0.85$). This is due to phase-slips (step-like changes in $\Delta\varphi(t)$ in Fig. 1F) between flagella and the flow, and means that the θ_t -flow synchronization is less stable. Additionally, for intermediate detuning ($0.5\text{ Hz} < |\nu| < 4\text{ Hz}$), $\tau(\theta_c)$ is always larger than $\tau(\theta_t)$. In some cases, the θ_c -flow synchronizes the cell fully whereas the θ_t -flow fails completely (e.g., at $\nu = -2\text{ Hz}$). Together, these results imply that a flow of given amplitude synchronizes flagellar beating more effectively if it selectively loads the *cis*.

We repeat the experiments with cells from multiple cultures, captured on different pipettes, and with different eyespot orientations ($\sim 50\%$ heading rightward in the imaging plane) to rule out possible influence from the setup. $\tau(\nu; \theta)$ of $N=11$ *wt* cells tested in the TRIS-minimal medium (pH=7.0) are displayed in Fig. 3B (labeled as "TRIS"). On average, $\varepsilon(\theta_c) = 2.9\text{ Hz}$ and is 70% larger than $\varepsilon(\theta_t) = 1.7\text{ Hz}$. It bears emphasis that $\varepsilon(\theta_c) > \varepsilon(\theta_t)$ holds true for every single cell tested (11/11). In Fig. 3C, we show this by representing each cell as a point in the $\varepsilon(\theta_c) - \varepsilon(\theta_t)$ plane. A point being below the first bisector line ($\varepsilon(\theta_c) = \varepsilon(\theta_t)$) indicates that $\varepsilon(\theta_c) > \varepsilon(\theta_t)$ for this cell. All cells cluster clearly below the line. This asymmetry manifest equivalently through τ . In Fig. 3D, each point represents the time fractions of the same cell synchronized by the θ_c -flow and the θ_t -flow at the same frequency. Most points ($>90\%$) are below the first bisector line, meaning that $\tau(\theta_c) > \tau(\theta_t)$. Altogether, all results show that selectively loading the *cis* flagellum establishes synchronization with the flow more effectively, pointing to *cis* and *trans* playing differential roles in the coordinated beating.

We next study whether this newly observed *cis-trans* asymmetry is affected by calcium depletion. Calcium is a critical second messenger for modulating flagellates motility and is deeply involved in phototaxis (45). The depletion of the free environmental calcium is known to degrade flagellar synchronization and exacerbate flagellar asymmetry (22). Here we focus on whether calcium depletion affects the asymmetry $\varepsilon(\theta_c) > \varepsilon(\theta_t)$. We deplete environmental calcium by EGTA-chelation, following the protocol in Ref. (46). Similar to previous reports (22, 47), the number of freely swimming cells drops significantly in EGTA-containing medium. However, the remaining cells beat synchronously for hours after capture. For these beating cells, calcium depletion is first confirmed by characterizing their deflagellation behavior. Indeed, calcium depletion is reported to inhibit deflagellation (28, 48). In experiments with standard calcium concentration, all cells deflagellated under pipette suction (20/20). For experiments

conducted in calcium depleting EGTA-containing medium, we observe deflagellation to occur in none but one cell (1/19).

After confirming the calcium depletion, we perform the same sets of flow synchronization experiments. The dashed lines in Fig. 3B show the median synchronization profiles $\tau(\nu; \theta)$ (N=6 cells, labeled as "EGTA"). The flagellar asymmetry is unaffected, see also Fig. 3E. Note that $\varepsilon(\theta_c) > \varepsilon(\theta_t)$ again applies for every single cell tested. The mean values of ε drop slightly. However, the different effectiveness between θ_c -flows and θ_t -flows, $\varepsilon(\theta_c) - \varepsilon(\theta_t)$, is not affected, see Fig. 3E inset.

Finally, we determine how the forcing strength of the flow depends on the hydrodynamic forces exerted by the flow on the flagella. We compute the hydrodynamic beat-averaged loads, $\overline{F}_{\text{Flow}} = \int_0^{2\pi} F_{\text{Flow}} d\varphi / 2\pi$, $\overline{P}_{\text{Flow}} = \int_0^{2\pi} P_{\text{Flow}} d\varphi / 2\pi$, induced by the flow on the *trans* and on the *cis* flagella, see the horizontal lines in Fig. 2. These loads are computed for the θ_c -flow, θ_t -flow, θ_a -flow and we also include experiments and computations performed with flows along $\theta = 90^\circ$ (circles), see **SM. Sec.S2**. Fig. 3F and G represent ε as a function of the loads on the *cis* and *trans* flagellum respectively, with each symbol representing one of the four different flow directions, see the drawings. We find that the effective forcing strength scales with the time-averaged drag on the *cis*, $\varepsilon \sim \overline{F}_{\text{Flow}}^c$, while we find no such correlation between ε and $\overline{F}_{\text{Flow}}^t$. The linear relation between ε and $\overline{F}_{\text{Flow}}^c$ has an intercept near zero ($\varepsilon|_{\overline{F}_{\text{Flow}}^c=0} \approx 0$). Given the total forces on both flagella ($\overline{F}_{\text{Flow}}^c + \overline{F}_{\text{Flow}}^t$) for these flows remains almost constant (0.74-0.79 F_0), the zero-intercept implies that for a hypothetical flow that exerts no load on the *cis* but solely forces the *trans*, it will not be able to synchronize the cell at all. This suggests a negligible contribution of the forcing on the *trans* in establishing synchronization with flows.

The asymmetry is lost in *ptx1* mutants

Furthermore, we examine the flagellar dominance mutant *ptx1*. In this mutant, both flagella respond similarly to changes of calcium concentrations (38) and have similar beating frequencies when demembranated and reactivated (23).

Ptx1 mutants have two modes of coordinated beating, namely, the in-phase (IP) synchronization and the anti-phase (AP) synchronization (29, 49). First, we apply θ_a -flow in the same frequency and amplitude ranges as for *wt* cells. We find that the IP mode around $f_0 \approx 50$ Hz is the only mode that can be synchronized by external flows. We focus on this mode and report τ as $\tau = t_{\text{sync}}/t_{\text{IP}}$ for this mutant, where t_{IP} is the total time of IP-beating under the applied

flows, see Fig. 4A. Synchronization profiles $\tau(\nu; \theta)$ of *ptxI* are shown in Fig. 4B. The median profiles are of similar width and height, indistinguishable from each other, and hence indicate a loss of asymmetric susceptibility to flow synchronization. The loss is further confirmed by the extracted $\varepsilon(\theta)$ (31) and $\tau(\theta)$ (Fig. 4C-D). Cells and synchronization attempts are distributed evenly across the first bisector lines (7/14 cells are below $\varepsilon(\theta_c) = \varepsilon(\theta_t)$ in Fig. 4C, and $\sim 50\%$ points are below $\tau(\theta_c) = \tau(\theta_t)$ in Fig. 4D). Altogether, all results show consistently that the asymmetry is lost in *ptxI*.

Modeling

Framework

To investigate the implications of our experimental results on the coupling between flagella and their dynamics, we develop a model for the system (**SM. Sec.S3**), representing flagella and external flows as oscillators with directional couplings:

$$\begin{cases} \dot{\varphi}_f = 2\pi f_f \\ \dot{\varphi}_c = 2\pi[f_c - \lambda_t \sin(\varphi_c - \varphi_t) - \varepsilon_c \sin(\varphi_c - \varphi_f)] + \zeta_c(t) \\ \dot{\varphi}_t = 2\pi[f_t - \lambda_c \sin(\varphi_t - \varphi_c) - \varepsilon_t \sin(\varphi_t - \varphi_f)] + \zeta_t(t). \end{cases} \quad (2)$$

$\varphi_{f,c,t}(t)$ respectively represent the phase of the flow, the *cis*, and the *trans* flagellum. $f_{f,c,t}$ represents the inherent frequency of the forcing (flow), the *cis*, and the *trans* respectively. The phase dynamics of each flagellum is modulated by its interactions with the other flagellum as well as the background flow. Take the *cis* ($\dot{\varphi}_c$) for example, the effect of the *trans* and the forcing on the *cis* are respectively accounted for by the λ_t -term and the ε_c -term, see Eq. (2). In other words, λ_t and ε_c measure the sensitivity of the actual *cis*-frequency to the phase differences between oscillators ($\varphi_c - \varphi_{t,f}$), see the arrows in Fig. 5A. Lastly, $\zeta_{c,t}$ represent the white noise of the *cis* and *trans* flagellum respectively. In the following parts, without loss of generality, the noise are assumed equally strong and uncorrelated ($\langle \zeta_c^2 \rangle = \langle \zeta_t^2 \rangle$, or $T_{\text{eff}}^c = T_{\text{eff}}^t$). Nuanced phase dynamics under differential noise levels can be found in **SM. Sec.S4**.

Eq. (2) can be readily reduced to Eq. (1), which allows us to write the experimentally measured values (f_0 , $\varepsilon(\theta)$, T_{eff}) analytically with $\varepsilon_{c,t}$, $\lambda_{c,t}$, and $\zeta_{c,t}$. The asymptotic behavior of the

model under the condition $\varphi_c \approx \varphi_t \approx \varphi_f$ are (**SM. Sec.S3**):

$$\begin{cases} f_0 &= \alpha f_c + (1 - \alpha) f_t, \\ T_{\text{eff}} &= \alpha^2 T_{\text{eff}}^c + (1 - \alpha)^2 T_{\text{eff}}^t, \\ \varepsilon(\theta) &= \alpha \varepsilon_c(\theta) + (1 - \alpha) \varepsilon_t(\theta), \end{cases} \quad (3)$$

with $\alpha = \lambda_c / (\lambda_c + \lambda_t)$ representing the dominance of *cis*. It is then clear that when $\alpha \approx 1$, the coordinated beating will display dynamic properties of the *cis* flagellum.

Fig. 5A illustrates an exemplary modeling scheme describing flagellar beating subjected to θ_c -flows. The direction and thickness of arrows represent coupling direction and strength respectively. The selective loading on the *cis* is represented by $\varepsilon_c > \varepsilon_t$; while $\lambda_c > \lambda_t$ reflects that the *cis* has a more dominant role in the coordinated beating. We run Monte-Carlo simulation with Eq. (2) using customized MATLAB scripts.

Coordinated beating under symmetric forcing

We first model the flow synchronization induced by θ_a -flow (symmetric flagellar loads). In this case, $\varepsilon(\theta) = \alpha \varepsilon_c(\theta) + (1 - \alpha) \varepsilon_t(\theta)$ (Eq. (3)) reduces to $\varepsilon = \varepsilon_{c,t}$ and is independent of α . We set $\varepsilon_{c,t}$ as 2.4 Hz to match the measured $\varepsilon(\theta_a) = 2.4$ Hz (Fig. 3B).

At similar detunings as in the experimental results in Fig. 1F, our Monte-Carlo simulations reproduces the phase dynamics with: (i) no flow synchronization, (ii-iii) unstable synchronization, and (iv) stable synchronization (Fig. 5B). Repeating the simulations for varying forcing strength $\varepsilon (= \varepsilon_{c,t})$ and frequency f_f yields Arnold tongue diagrams in agreement with those reported from our experiments. The Arnold Tongue for *wt* in Fig. 3A and *ptx1* in Fig. 4A are reproduced with simulations shown in Fig. 5C and D respectively. The only parameter value changed between Fig. 5C and D is the level of noise ($T_{\text{eff}}^{c,t}$), which is increased by an order of magnitude. The differences in phase dynamics between *wt* and *ptx1*, when subjected to symmetric external loading, are therefore accounted by solely varying the noise.

Coordinated beating under selective loading

We next model flow synchronization by the θ_c -flows and the θ_t -flows. The selective forcing ($\varepsilon_c \neq \varepsilon_t$) allows the effect of flagellar dominance ($\lambda_c \neq \lambda_t$) to manifest in the effective forcing strength $\varepsilon(\theta)$ and hence in the synchronization profiles $\tau(\nu; \theta)$, Fig. 5E. Similar to our experimental observations, θ_c -flow synchronizes the coordinated beating over the broadest range of ν (i.e. largest ε). This is directly attributed to the dominance $\lambda_c > \lambda_t$: by setting $\lambda_c = \lambda_t$,

the differences between $\tau(\theta_c)$ and $\tau(\theta_t)$ disappear even under selective loading (Fig. 5E inset). Fig. 5F details how the asymmetry of inter-flagellar coupling (λ_c/λ_t) affects the asymmetry between $\tau(\theta_c)$ and $\tau(\theta_t)$. The open symbols represent $\varepsilon(\theta)$ measured from modeled $\tau(\nu; \theta)$ and the lines represent Eq. (3). The difference between $\varepsilon(\theta_c)$ and $\varepsilon(\theta_t)$ increases with λ_c/λ_t , and they each saturates to reflect only the forcing on the *cis* (ε_c , the grey dashed lines). With $f_c = 45$ Hz, $f_t = 65$ Hz (23, 26), and $f_0 \approx 50$ Hz, we deduce from Eq. (3) that $\lambda_c = 4\lambda_t$ for *wt* cells. For *wt* cells under calcium depletion, experimental results are reproduced with a lower total forcing strength (Fig. 5G). $\varepsilon_c + \varepsilon_t$ is set to 4.08 Hz (15% lower) to reflect the 7% – 20% decrease in $\varepsilon(\theta)$ induced by calcium depletion.

The *ptx1* results are reproduced with a stronger noise ($T_{\text{eff}}^{c,t} = 9.42 \text{ rad}^2/\text{s}$) and a symmetric inter-flagellar coupling $\lambda_c/\lambda_t = 1$, see Fig. 5H and **Table. 1**. Both changes are necessary for reproducing the synchronization profiles of *ptx1* in Fig. 5H: while the stronger noise lowers the maximal values of $\tau(\theta, \nu)$, setting $\lambda_c/\lambda_t = 4$ would still result in $\tau(\theta_c) > \tau(\theta_t)$ in the central range ($|\nu| \lesssim 2.4$ Hz). Finally, it is noteworthy that the noise in *ptx1* increases not only because a higher noise value for individual flagella, but also because the *cis-trans* coupling has become symmetric. As shown by Eq. (3), the unilateral coupling promotes not only the *cis*-frequency in the synchrony but also the *cis*-noise. Given $T_{\text{eff}}^c \ll T_{\text{eff}}^t$ and $\lambda_c = 4\lambda_t$, we confirm with simulations that the *cis* stabilizes the beating frequency of the *trans* and decreases its beating noise. The simulations are in good agreement with experimental noise measurements, see **SM. Sec.S4** for details.

Discussion

The two flagella of *C. reinhardtii* have long been known to have inherently different dynamic properties such as frequency, waveform, level of active noise, and responses to second messengers (23, 25, 26, 29, 30). Intriguingly, when connected by basal fibers and beating synchronously, they both adopt the kinematics of the *cis*-(eyespot) flagellum, which led to the assumption that the flagella may have differential roles in coordination. In this work, we test this hypothesis by employing oscillatory flows applied from an angle with respect to the cells' symmetry axis and thus exert biased loads on one flagellum.

Without an exception, in *wt* cells, θ_c -flows, the ones that selectively load the *cis* flagellum, are always more effective in synchronizing the flagellar beating than the θ_t -flows. This is shown by the larger effective forcing strengths ($\varepsilon(\theta_c) > \varepsilon(\theta_t)$), Fig. 3B-C) and larger synchronized time

fractions ($\tau(\theta_c) > \tau(\theta_t)$, Fig. 3D). Mapping the measured forcing strength $\varepsilon(\theta)$ as a function of the loads, we find empirically that $\varepsilon \propto \overline{F}_{\text{Flow}}^c$ (Fig. 3F) and that *trans*-loads appear to matter negligibly. These observations all indicate that the *cis*-loads determine whether an external forcing can synchronize the cell. Moreover, this point is further highlighted by an unexpected finding: when θ_t -flows are applied, the *trans* flagellum always beats against the external flow ($P_{\text{Flow}}^t < 0$) and the only stabilizing factor for flow synchronization is the *cis* flagellum working along with the flow during the recovery stroke (Fig. 2C lower panel). These observations definitively prove that the two flagella have differential roles in the coordination and interestingly imply that flagella are coupled to external flow only through the *cis*.

To have a mechanistic understanding of this finding, we model the system with Eq. (2). In the model, selective hydrodynamic loading and flagellar dominance in the coordinated beating are respectively represented by $\varepsilon_c \neq \varepsilon_t$ and $\lambda_c \neq \lambda_t$. Setting out from the model, we obtain closed-form expressions for observables such as f_0 and ε (Eq. (3)), which illustrate how flagellar dominance and selective loading affect the coordinated flagellar beating. Moreover, with Monte-Carlo simulation, we clarified the interplay between flows and flagella (**SM. Sec.S3**), and reproduces all experimental observations.

With the model, we show that a "dominance" of the *cis* ($\lambda_c > \lambda_t$) is sufficient to explain why the coordinated flagellar beating bears the frequency and the noise level of the *cis* flagellum. In the model, such dominance means that the *cis*-phase is much less sensitive to the *trans*-phase than the other way around. We then reproduce the phase dynamics of flow synchronization at varying detunings (Fig. 5B), amplitudes (Fig. 5C), and noise (Fig. 5D). Exploiting the observation that the coordination between flagella cannot be broken by external flows up to the strongest ones tested ($\varepsilon^{\max} \sim 10$ Hz, Fig. 3A), we quantify the lower limit of the total basal coupling, $\lambda_c + \lambda_t$, to be approximately 40 Hz (deduced in **SM. Sec.S3**), which is an order magnitude larger than the hydrodynamic inter-flagellar coupling (31, 50–52).

The modulation of flagellar dominance mediates tactic behaviors (22, 23, 38, 47). Calcium is hypothesized to be underlying the modulation of dominance, as it causes the connecting fiber between flagella to contract (53), modulates the *cis*- and *trans* activity (e.g. beating amplitude) differentially (22), and calcium influx comprises the initial step of CR's photo- (54) and mechanoresponses (45). We therefore investigate flagellar coupling in the context of tactic steering by depleting the environmental free calcium and hence inhibiting signals of calcium influxes. Cells are first acclimated to calcium depletion, and then tested with the directional flows. Our results show that the *cis* dominance does not require the involvement of free envi-

ronmental calcium. Calcium depletion merely induces an overall drop in the forcing strength perceived by the cell $\varepsilon(\theta)$ (7% – 20%), which is captured by reducing $\varepsilon_c + \varepsilon_t$ for 15% (mean drop) in the model (Fig. 5G). Together, our results indicate that the leading role of *cis*, is an inherent property, that does not require active influx of external calcium, and possibly reflects an intrinsic mechanical asymmetry of the cellular mesh that anchors the two flagella into the cell body.

In *ptxI* cells, a lack of flagellar dominance ($\lambda_c = \lambda_t$) and a stronger noise level help reproduce our experimental observations. Previous studies suggested that both flagella of *ptxI* are similar to the wildtype *trans* (23), and that the noise levels of this mutant’s synchronous beating are much greater than those of *wt* (29) (see also **SM. Sec.S4**). If both flagella and their anchoring roots indeed have the composition of the wildtype *trans*, such symmetry would predict $\lambda_c = \lambda_t$. This symmetric coupling renders the noise of *ptxI* $T_{\text{eff}} = T_{\text{eff}}^t$ (Eq. (3)), which is about an order of magnitude larger than the noise of *wt* $T_{\text{eff}} \approx T_{\text{eff}}^c$.

The comparison between *ptxI* and *wt* highlights an intriguing advantage of the observed unilateral coupling ($\lambda_c \gg \lambda_t$); that is, it strongly suppresses the high noise of the *trans*. Considering that the *trans* is richer in CAH6 protein and this protein’s possible role in inorganic carbon sensing (14, 20), the potential sensing role of the *trans* is worth noticing. Assuming the strong noise present in the *trans* originates from the biochemical processes related to sensing, then the unilateral coupling effectively prevents such noise from perturbing the cell’s synchronous beating and effective swimming. In this way, the asymmetric coupling may combine the benefit of having a stable *cis* as the driver while equipping a noisy *trans* as a sensor.

Material and methods

Cell culture

CR wildtype (*wt*) strain cc125 (mt+) and flagellar dominance mutant *ptxI* cc2894 (mt+) are cultured in TRIS-minimal medium (pH=7.0) with sterile air bubbling, in a 14h/10h day-night cycle. Experiments are performed on the 4th day after inoculating the liquid culture, when the culture is still in the exponential growth phase and has a concentration of $\sim 2 \times 10^5$ cells/ml. Before experiments, cells are collected and resuspended in fresh TRIS-minimal (pH=7.0).

Calcium depletion

In calcium depletion assays, cells are cultured in the same fashion as mentioned above but washed and resuspended in fresh TRIS-minimal medium + 0.5 mM EGTA (pH=7.0). Free calcium concentration is estimated to drop from 0.33 mM in the TRIS-minimal medium, to 0.01 μ M in the altered medium (46). Experiments start at least one hour after the resuspension in order to acclimate the cells.

Experimental setup

Single cells of CR are studied following a protocol similar to the one described in (31). Cell suspensions are filled into a customized flow chamber with an opening on one side. The air-water interface on that side is pinned on all edges and is sealed with silicone oil. A micropipette held by micromanipulator (SYS-HS6, WPI) enters the chamber and captures single cells by aspiration. The manipulator and the captured cell remain stationary in the lab frame of reference, while the flow chamber and the fluid therein are oscillated by a piezoelectric stage (Nano-Drive, Mad City Labs), such that external flows are applied to the cell. Frequencies and amplitudes of the oscillations are individually calibrated by tracking micro-beads in the chamber. Bright field microscopy is performed on an inverted microscope (Nikon Eclipse Ti-U, 60 \times water immersion objective). Videos are recorded with a sCMOS camera (LaVision PCO.edge) at 600-1000 Hz.

Measurement scheme

The flagellar beating of each tested cell is recorded before, during, and after the application of the flows. We measure the cell's average beating frequency f_0 over 2 s (~ 100 beats). For *ptx1* cells, f_0 is reported for the in-phase (IP) synchronous beating. Unless otherwise stated, directional flows ($\theta = 0, \pm 45^\circ$) are of the same amplitude ($780 \pm 50 \mu\text{m/s}$, mean \pm std), similar to those used in Ref. (31). Flow frequencies f_f are scanned over $[f_0 - 7, f_0 + 7]$ Hz for each group of directional flows.

Computation of the flagellar loads

To quantify the hydrodynamic forces on the flagella, we first track realistic flagellar deformation from videos wherein background flows are applied. Then we employ a hybrid method combining boundary element method (BEM) and slender-body theory (40, 55) to compute the

drag forces exerted on each flagellum and the forces' rates of work. In this approach, each flagellum is represented as a slender-body (55) with 26 discrete points along its centerline and the time-dependent velocity of each of the 26 points is calculated by its displacement across frames. The cell body and the pipette used to capture the cell are represented as one entity with a completed double layer boundary integral equation (56). Stresslet are distributed on cell-pipette's surface; while stokeslet and rotlet of the completion flow are distributed along cell-pipette's centerline (57). The no-slip boundary condition on the cell-pipette surface is satisfied at collocation points. Lastly, stokeslets are distributed along the centerlines of the flagella, so that no-slip boundary conditions are met on their surfaces. Integrating the distribution of stokeslets $\mathbf{f}(s)$ over a flagellar shape, one obtains the total drag force $\mathbf{F} = \int \mathbf{f}(s)ds$ is obtained. Similarly, the force's rate of work is computed as $P = \int \mathbf{f}(s) \cdot \mathbf{U}(s)ds$, where $\mathbf{U}(s)$ is the velocity of the flagellum at the position s along the centerline.

The computations shown in this study are based on videos of a representative cell which originally beats at ~ 50 Hz. The cell is fully synchronized by flows along different directions ($\theta = 0^\circ, \pm 45^\circ$ and 90°) at 49.2 Hz. In the computations, the applied flows are set to have an amplitude of $780 \mu\text{m/s}$ to reflect the experiments. Computations begin with the onset of the background flows (notified experimentally by a flashlight event), and last for ~ 30 beats (500 frames sampled at 801 fps). Additionally, we confirm the results of θ_t -flow-synchronization, that both flagella spend large fractions of time beating against the flows, with other cells and with θ_t -flows at other frequencies.

Isolate loads of external flows

The total loads (\mathbf{F} and P) computed consist of two parts, one from the flow created by the two flagella themselves and the other from the applied flow. In the low Reynolds number regime, the loads of the two parts add up directly (linearity): $\mathbf{F} = \mathbf{F}_{\text{Self}} + \mathbf{F}_{\text{Flow}}$, and $P = P_{\text{Self}} + P_{\text{Flow}}$. To isolate \mathbf{F}_{Flow} and P_{Flow} , we compute $\mathbf{F}' = \mathbf{F}_{\text{Self}}$ and $P' = P_{\text{Self}}$ by running the computation again but without the external flows, and obtain $\mathbf{F}_{\text{Flow}} = \mathbf{F} - \mathbf{F}'$ and $P_{\text{Flow}} = P - P'$.

Modeling parameters

We assume the flagellar intrinsic frequencies f_c and f_t to be 45 Hz and 65 Hz respectively (23, 26, 28). On this basis, $\lambda_c : \lambda_t$ is assumed to be 4:1 to account for the observed f_0 (~ 50 Hz). $\varepsilon_c : \varepsilon_t$ is set as 2:1, 1:1, and 1:2 for the θ_c -flows, the θ_a -flows, and the θ_t -flows respectively,

see Fig. 2A-C. Additionally, $\varepsilon_c + \varepsilon_t$ is assumed to be constant to reflect the fact that $\overline{F}_{\text{Flow}}^c + \overline{F}_{\text{Flow}}^t$ approximately does not vary with flow directions. We take a typical value of $T_{\text{eff}}^{c,t} = 1.57 \text{ rad}^2/\text{s}$ (31). The sum of inter-flagellar coupling $\lambda_{\text{tot}} = \lambda_c + \lambda_t$ is set to be large enough, i.e., $\lambda_{\text{tot}} = 3\nu_{\text{ct}}$ with $\nu_{\text{ct}} = |f_t - f_c|$, to account for the fact that: 1) the coordinated beating is approximated in-phase, and 2) up until the strongest flow applied, the coordinated beating cannot be broken (quantitative evaluation is detailed in **SM. Sec.S3**). To model *wt* cells under calcium depletion, we decrease $\varepsilon_c + \varepsilon_t$ by 15% - which is the mean decrease in the observed $\varepsilon(\theta_c)$, $\varepsilon(\theta_a)$, and $\varepsilon(\theta_t)$ (Fig. 3E). For *ptx1* cells, we assume a symmetric inter-flagellar coupling ($\lambda_c = \lambda_t$) and a stronger noise level (**SM. Sec.S4**). The parameters are summarized in **Table. 1**.

Table 1: Modeling parameters

variable	symbol (unit)	TRIS	EGTA	<i>ptx1</i>
Intrinsic freq. (23, 26)	f_c, f_t (Hz)	45,65	45,65	45,65
Basal coupling*	$\lambda_c + \lambda_t$ (Hz)	60	60	60
<i>cis</i> dominance (23, 38)	$\lambda_c : \lambda_t$ (-)	4:1	4:1	1:1
Flow detuning	ν (Hz)	[-10,10]	[-10,10]	[-10,10]
Total forcing (51)	$\varepsilon_c + \varepsilon_t$ (Hz)	4.8	4.08	4.8
Noise* (31)	$T_{\text{eff}}^{c,t}$ (rad^2/s)	1.57	1.57	9.42

* detailed in **SM. Sec.S3**

References

1. Berg, H. C. & Brown, D. A. Chemotaxis in *Escherichia coli* analysed by three-dimensional tracking. *Nature* **239**, 500–504 (1972).
2. Smriga, S., Fernandez, V. I., Mitchell, J. G. & Stocker, R. Chemotaxis toward phytoplankton drives organic matter partitioning among marine bacteria. *Proceedings of the National Academy of Sciences* **113**, 1576–1581 (2016).
3. Hegemann, P. & Berthold, P. Chapter 13 - sensory photoreceptors and light control of flagellar activity. In Harris, E. H., Stern, D. B. & Witman, G. B. (eds.) *The Chlamydomonas Sourcebook (Second Edition)*, vol. 3, 395–429 (Academic Press, London, 2009).
4. Ueki, N., Matsunaga, S., Inouye, I. & Hallmann, A. How 5000 independent rowers coordinate their strokes in order to row into the sunlight: Phototaxis in the multicellular green alga *Volvox*. *BMC Biology* **8**, 103 (2010).
5. Stehnach, M. R., Waisbord, N., Walkama, D. M. & Guasto, J. S. Viscophobic turning dictates microalgae transport in viscosity gradients. *Nature Physics* **17**, 926–930 (2021).
6. Brokaw, C., Josslin, R. & Bobrow, L. Calcium ion regulation of flagellar beat symmetry in reactivated sea urchin spermatozoa. *Biochemical and Biophysical Research Communications* **58**, 795–800 (1974).
7. Gong, A. *et al.* The steering gaits of sperm. *Philosophical Transactions of the Royal Society B: Biological Sciences* **375**, 20190149 (2020).
8. Gadêlha, H., Hernández-Herrera, P., Montoya, F., Darszon, A. & Corkidi, G. Human sperm uses asymmetric and anisotropic flagellar controls to regulate swimming symmetry and cell steering. *Science Advances* **6**, eaba5168 (2020).
9. Bennett, R. R. & Golestanian, R. A steering mechanism for phototaxis in *Chlamydomonas*. *Journal of The Royal Society Interface* **12**, 20141164 (2015).
10. Rüffer, U. & Nultsch, W. Flagellar photoresponses of *Chlamydomonas* cells held on micropipettes: II. Change in Flagellar Beat Pattern. *Cell Motility and the Cytoskeleton* **18**, 269–278 (1991).

11. Ueki, N. & Wakabayashi, K.-i. Dynein-mediated photobehavioral responses in *Chlamydomonas*. In *Dyneins*, 368–385 (Elsevier Ltd., 2017), second edition edn.
12. Naitoh, Y. & Kaneko, H. Reactivated triton-extracted models of paramecium: Modification of ciliary movement by calcium ions. *Science* **176**, 523–524 (1972).
13. Merchant, S. S. *et al.* The *Chlamydomonas* genome reveals the evolution of key animal and plant functions. *Science* **318**, 245–250 (2007).
14. Choi, H. I., Kim, J. Y. H., Kwak, H. S., Sung, Y. J. & Sim, S. J. Quantitative analysis of the chemotaxis of a green alga, *Chlamydomonas reinhardtii*, to bicarbonate using diffusion-based microfluidic device. *Biomicrofluidics* **10**, 014121–014121 (2016).
15. Rüffer, U. & Nultsch, W. Flagellar photoresponses of *Chlamydomonas* cells held on micropipettes: I. change in flagellar beat frequency. *Cell Motility and the Cytoskeleton* **15**, 162–167 (1990).
16. Holmes, J. & Dutcher, S. Cellular asymmetry in *C. reinhardtii*. *Journal of Cell Science* **94**, 273–285 (1989).
17. Dutcher, S. K. & O'Toole, E. T. The basal bodies of *C. reinhardtii*. *Cilia* **5**, 1–7 (2016).
18. Mittelmeier, T. M., Boyd, J. S., Lamb, M. R. & Dieckmann, C. L. Asymmetric properties of the *Chlamydomonas reinhardtii* cytoskeleton direct rhodopsin photoreceptor localization. *Journal of Cell Biology* **193**, 741–753 (2011).
19. Sakakibara, H., Mitchell, D. R. & Kamiya, R. A *Chlamydomonas* outer arm dynein mutant missing the alpha heavy chain. *The Journal of cell biology* **113**, 615–622 (1991).
20. Mackinder, L. C. *et al.* A spatial interactome reveals the protein organization of the algal CO₂-concentrating mechanism. *Cell* **171**, 133–147.e14 (2017).
21. Yu, K., Liu, P., Venkatachalam, D., Hopkinson, B. M. & Lehtreck, K. F. The bbsome restricts entry of tagged carbonic anhydrase 6 into the cis-flagellum of *chlamydomonas reinhardtii*. *PLOS ONE* **15**, 1–21 (2020).
22. Kamiya, R. & Witman, G. B. Submicromolar levels of calcium control the balance of beating between the two flagella in demembrated models of *Chlamydomonas*. *Journal of Cell Biology* **98**, 97–107 (1984).

23. Okita, N., Isogai, N., Hirono, M., Kamiya, R. & Yoshimura, K. Phototactic activity in *Chlamydomonas* 'non-phototactic' mutants deficient in Ca^{2+} -dependent control of flagellar dominance or in inner-arm dynein. *Journal of Cell Science* **118**, 529–537 (2005).
24. Takada, S. & Kamiya, R. Beat frequency difference between the two flagella of *Chlamydomonas* depends on the attachment site of outer dynein arms on the outer-doublet microtubules. *Cell Motility and the Cytoskeleton* **36**, 68–75 (1997).
25. Saegusa, Y. & Yoshimura, K. cAMP controls the balance of the propulsive forces generated by the two flagella of *Chlamydomonas*. *Cytoskeleton* **72**, 412–421 (2015).
26. Kamiya, R. & Hasegawa, E. Intrinsic difference in beat frequency between the two flagella of *Chlamydomonas reinhardtii*. *Experimental Cell Research* **173**, 299–304 (1987).
27. Ruffer, U. & Nultsch, W. Comparison of the beating of *cis*- and *trans*-flagella of *Chlamydomonas* cells held on micropipettes. *Cell Motility and the Cytoskeleton* **7**, 87–93 (1987).
28. Wan, K. Y., Leptos, K. C. & Goldstein, R. E. Lag, lock, sync, slip: the many phases of coupled flagella. *Journal of The Royal Society Interface* **11**, 20131160 (2014).
29. Leptos, K. C. *et al.* Antiphase synchronization in a flagellar-dominance mutant of *Chlamydomonas*. *Physical Review Letters* **111**, 1–5 (2013).
30. Wan, K. Y. Coordination of eukaryotic cilia and flagella. *Essays In Biochemistry* **62**, 829–838 (2018).
31. Quaranta, G., Aubin-Tam, M.-E. & Tam, D. Hydrodynamics versus intracellular coupling in the synchronization of eukaryotic flagella. *Physical Review Letters* **115**, 238101 (2015).
32. Wan, K. Y. & Goldstein, R. E. Coordinated beating of algal flagella is mediated by basal coupling. *Proceedings of the National Academy of Sciences* **113**, E2784–E2793 (2016).
33. Ruffer, U. & Nultsch, W. High-speed cinematographic analysis of the movement of *Chlamydomonas*. *Cell Motility* **5**, 251–263 (1985).
34. Klindt, G. S., Ruloff, C., Wagner, C. & Friedrich, B. M. In-phase and anti-phase flagellar synchronization by waveform compliance and basal coupling. *New Journal of Physics* **19**, 113052 (2017).

35. Liu, Y. *et al.* Transitions in synchronization states of model cilia through basal connection coupling. *Journal of The Royal Society Interface* **15** (2018).
36. Guo, H., Man, Y., Wan, K. Y. & Kanso, E. Intracellular coupling modulates biflagellar synchrony. *Journal of The Royal Society Interface* **18**, 20200660 (2021).
37. Wan, K. Y. & Goldstein, R. E. Rhythmicity, recurrence, and recovery of flagellar beating. *Phys. Rev. Lett.* **113**, 238103 (2014).
38. Horst, J. & Witman, G. B. *Ptx1*, a nonphototactic mutant of *Chlamydomonas*, lacks control of flagellar dominance. *The Journal of Cell Biology* **120**, 733–741 (1993).
39. Wei, D., Dehnavi, P. G., Aubin-Tam, M.-E. & Tam, D. Is the zero reynolds number approximation valid for ciliary flows? *Physical Review Letters* **122**, 124502 (2019).
40. Wei, D., Dehnavi, P. G., Aubin-Tam, M.-E. & Tam, D. Measurements of the unsteady flow field around beating cilia. *Journal of Fluid Mechanics* **915**, A70 (2021).
41. Kralemann, B., Cimponeriu, L., Rosenblum, M., Pikovsky, A. & Mrowka, R. Phase dynamics of coupled oscillators reconstructed from data. *Phys. Rev. E* **77**, 066205 (2008).
42. Pikovsky, A., Rosenblum, M. & Kurths, J. *Synchronization: A Universal Concept in Non-linear Sciences*. Cambridge Nonlinear Science Series (Cambridge University Press, 2001).
43. Polin, M., Tuval, I., Drescher, K., Gollub, J. P. & Goldstein, R. E. *Chlamydomonas* swims with two “gears” in a eukaryotic version of run-and-tumble locomotion. *Science* **325**, 487–490 (2009).
44. Friedrich, B. Hydrodynamic synchronization of flagellar oscillators. *The European Physical Journal Special Topics* **225**, 2353–2368 (2016).
45. Yoshimura, K. *Stimulus Perception and Membrane Excitation in Unicellular Alga Chlamydomonas*, 79–91 (Springer Berlin Heidelberg, Berlin, Heidelberg, 2011).
46. Wakabayashi, K.-i., Ide, T. & Kamiya, R. Calcium-dependent flagellar motility activation in *C. reinhardtii* in response to mechanical agitation. *Cell Motility and the Cytoskeleton* **66**, 736–742 (2009).

47. Pazour, G. J., Agrin, N., Leszyk, J. & Witman, G. B. Proteomic analysis of a eukaryotic cilium. *The Journal of Cell Biology* **170**, 103–113 (2005).
48. Quarmby, L. & Hartzell, H. Two distinct, calcium-mediated, signal transduction pathways can trigger deflagellation in *C. reinhardtii*. *The Journal of Cell Biology* **124**, 807–815 (1994).
49. Rüffer, U. & Nultsch, W. Flagellar coordination in *Chlamydomonas* cells held on micropipettes. *Cell Motility and the Cytoskeleton* **41**, 297–307 (1998).
50. Brumley, D. R., Wan, K. Y., Polin, M. & Goldstein, R. E. Flagellar synchronization through direct hydrodynamic interactions. *eLife* **3**, e02750 (2014).
51. Klindt, G. S., Ruloff, C., Wagner, C. & Friedrich, B. M. Load response of the flagellar beat. *Physical Review Letters* **258101**, 1–5 (2016).
52. Pellicciotta, N. *et al.* Entrainment of mammalian motile cilia in the brain with hydrodynamic forces. *Proceedings of the National Academy of Sciences* **117**, 8315–8325 (2020).
53. Hayashi, M., Yagi, T., Yoshimura, K. & Kamiya, R. Real-time observation of Ca^{2+} -induced basal body reorientation in *Chlamydomonas*. *Cell Motility and the Cytoskeleton* **41**, 49–56 (1998).
54. Harz, H. & Hegemann, P. Rhodopsin-regulated calcium currents in *Chlamydomonas*. *Nature* **351**, 489–491 (1991).
55. Keller, J. B. & Rubinow, S. I. Slender-body theory for slow viscous flow. *Journal of Fluid Mechanics* **75**, 705–714 (1976).
56. Power, H. & Miranda, G. Second kind integral equation formulation of stokes' flows past a particle of arbitrary shape. *SIAM Journal on Applied Mathematics* **47**, 689–698 (1987).
57. Keaveny, E. E. & Shelley, M. J. Applying a second-kind boundary integral equation for surface tractions in stokes flow. *Journal of Computational Physics* **230**, 2141 – 2159 (2011).
58. Kamiya, R. Analysis of cell vibration for assessing axonemal motility in *Chlamydomonas*. *Methods* **22**, 383–387 (2000).

Acknowledgments

The authors thank Roland Kieffer for technical support. D.W. thanks Ritsu Kamiya for helpful discussions. The authors acknowledge support by the European Research Council (ERC starting grants no. 716712 and no. 101042612).

Author Contributions

D.W. performed experiments, computations, designed the model, and drafted the manuscript. G.Q. performed early experiments and obtained preliminary results. M.A. and D.T. conceived the study, supervised the project and critically revised the manuscript.

Competing interests

Authors declare that they have no competing interests.

Supplementary materials

Supplementary Text

Figs. S1 to S5

References (23, 26, 28, 29, 31, 38, 43, 58)

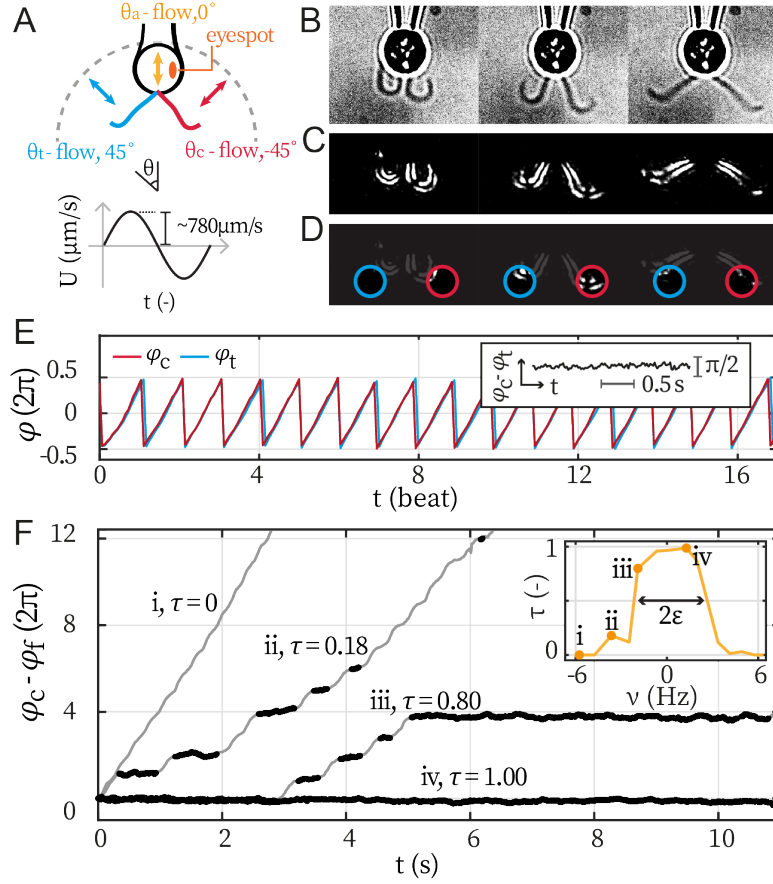


Figure 1: Experimental workflow. (A) Captured CR cells are subjected to sinusoidal flows of frequency f_f along given angles (θ) in the xy -plane. Flows along $\theta = -45^\circ, 0^\circ, 45^\circ$ of same amplitude ($780 \pm 50 \mu\text{m/s}$, mean \pm std.) are used and termed as shown. (B-E) Extracting flagellar phase φ_c and φ_t by image processing. Raw images (B) are thresholded and contrast-adjusted to highlight the flagella (C). Mean pixel values within the user-defined interrogation windows (red and blue circles) capture the raw phases of beating (D), which are then converted to observable-independent phases (E). Inset: phase difference $\varphi_c - \varphi_t$. (F) Flagella-flow phase dynamics at decreasing detuning $\nu = f_f - f_0$ with f_0 the cell's beating frequency without external flow. Traces i to iv are taken at detunings marked in the inset. Plateaus marked black represent flow synchronization, whose time fractions $\tau = t_{\text{sync}}/t_{\text{tot}}$ are noted. t_{tot} is the total time of recording. Inset: the flow synchronization profile, $\tau(\nu)$, reports the effective forcing strength 2ε by its width.

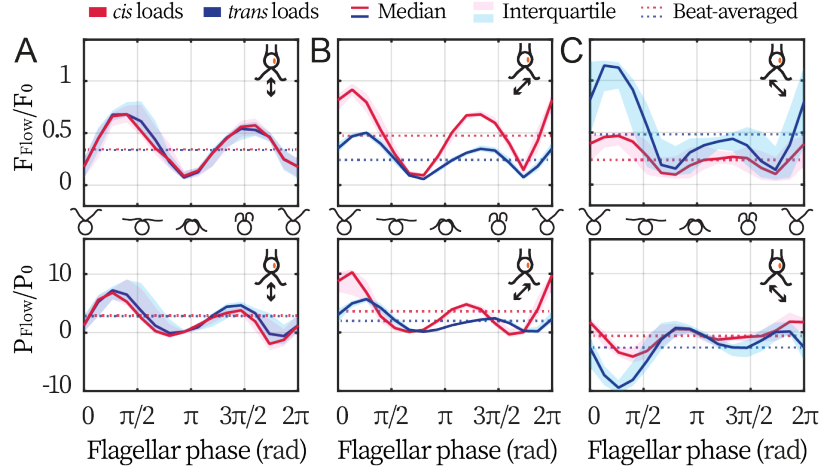


Figure 2: External flagellar loads when beating is synchronized. Force magnitude (upper panels) and power (lower panels) exerted by external flows of $\theta = 0^\circ$ (A, θ_a -flow), -45° (B, θ_c -flow), and $+45^\circ$ (C, θ_t -flow). The medians (solid lines) and interquartile ranges (shadings) are computed over ~ 20 synchronized beats. Dashed horizontal lines: loads averaged over a synchronized beat. Force magnitudes and powers are scaled by $F_0=9.9$ pN and $P_0=1.1$ fW respectively. Flagellar phase corresponds to the displayed shapes in the middle x -axis.

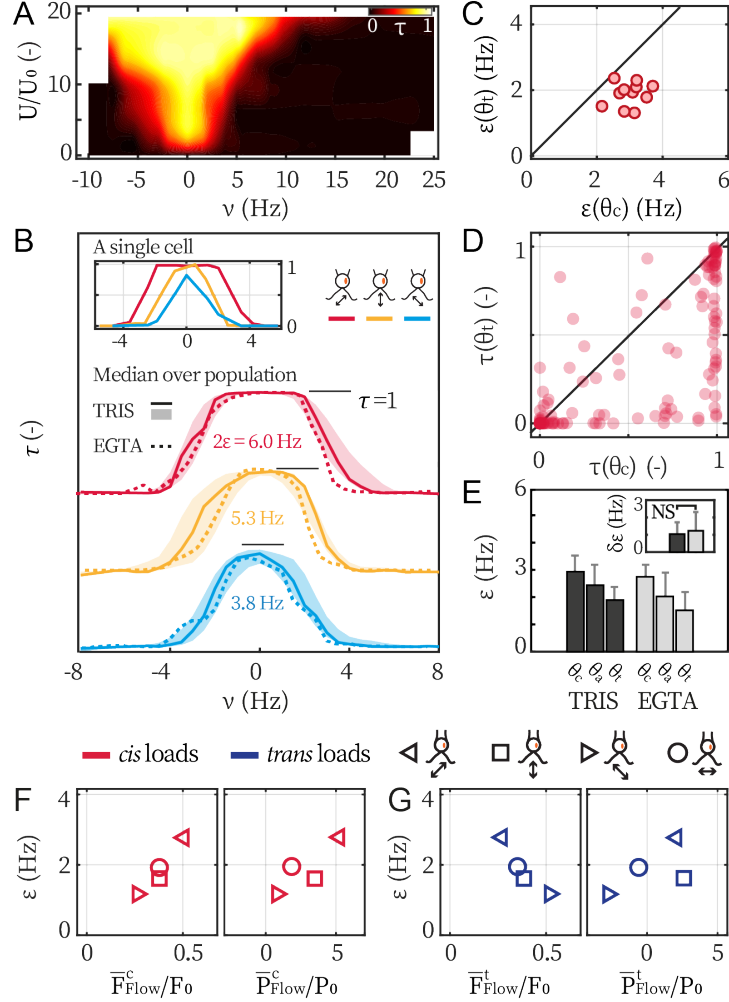


Figure 3: Flow synchronization of *wt* cells. (A) Arnold tongue of a representative cell tested with θ_a -flow. The contour is interpolated from $N=132$ measurements (6 equidistant amplitudes \times 22 equidistant frequencies), and color-coded by the entrained time fraction τ . (B) The synchronization profiles $\tau(\nu; \theta)$ of a representative *wt* cell (inset), the median profile of the TRIS group *wt* cells ($N=11$, solid lines) and the EGTA group ($N=6$, dashed lines), with either θ_c -flows (red), θ_a -flows (yellow) or θ_t -flows (blue). Shaded areas are the interquartile ranges for the TRIS group. (C) Tested *wt* cells represented on the $\varepsilon(\theta_c) - \varepsilon(\theta_t)$ plane (TRIS group). Solid line: the first bisector line ($y = x$). (D) Comparing $\tau(\nu; \theta_c)$ and $\tau(\nu; \theta_t)$ for each cell at each applied frequency. $N=132$ pairs of experiments are represented on the $\tau(\theta_c) - \tau(\theta_t)$ plane. More than 90% of them are below the first bisector line. (E) The coupling strengths $\varepsilon(\theta)$ of the TRIS group (black) and the EGTA group (gray). Bars and error bars: mean and 1 std., respectively. Inset: $\delta\varepsilon = \varepsilon(\theta_c) - \varepsilon(\theta_t)$. NS: not significant, $p > 0.05$, Kruskal-Wallis test, One-Way ANOVA. Relations between the forcing strength ε and the loads on the *cis* (F) and the *trans* flagellum (G). Markers represent different flow angles, see the drawings.

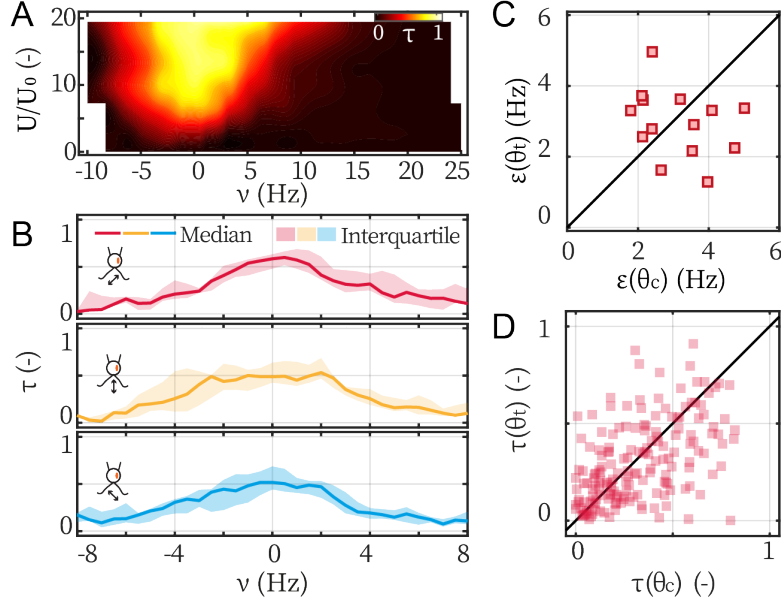


Figure 4: The asymmetric susceptibility to flow synchronization is lost in the flagellar dominance mutant *ptxI*. (A) Arnold tongue of a representative *ptxI* cell tested with θ_a -flow. The contour is interpolated from $N=132$ measurements (6 equidistant amplitudes \times 22 equidistant frequencies). Color bar: the entrained time fraction $\tau = t_{\text{sync}}/t_{\text{IP}}$. (B) Flow synchronization profiles $\tau(\nu; \theta)$ of $N=14$ *ptxI* cells, tested with θ_c -flows (red), θ_a -flows (yellow) and θ_t -flows (blue). (C) $\varepsilon(\theta_c)$ and $\varepsilon(\theta_t)$ of the tested cells. The first bisector line (solid): $y = x$. (D) $\tau(\nu; \theta_{c,t})$ for each cell at each applied frequency. $N=154$ points are present.

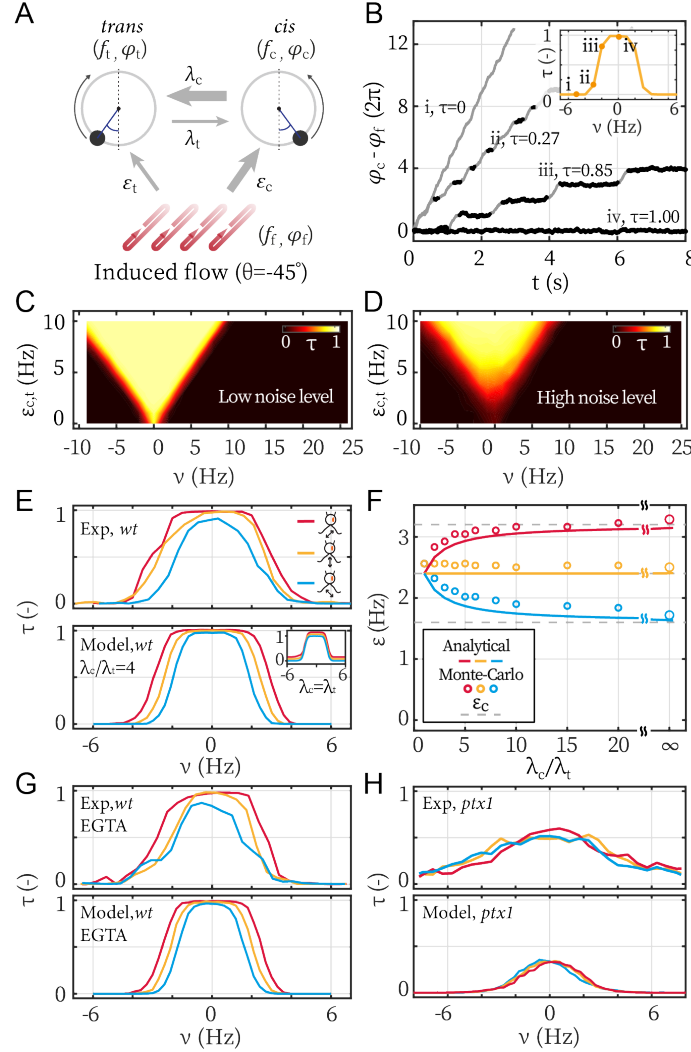


Figure 5: Modeling the asymmetric flow synchronization. (A) Modeling scheme describing a cell beating under directional flow (θ_c -flow as an example). Arrows represent the directional coupling coefficients with line thickness representing the relative strength. For example, λ_c points from *cis* to *trans*, representing how the latter (φ_c) is sensitive to the former (φ_t); meanwhile, the arrow of λ_c being thicker than λ_t means that φ_t is much more sensitive to φ_c than the other way around. (B) Modeled phase dynamics of flow synchronization under θ_a -flows, analogous to Fig. 1F. Reproducing the Arnold tongue diagrams at the noise level of *wt* (C) and *ptx1* (D), analogous to Fig. 3A and Fig. 4A respectively. (E) Flow synchronization profiles $\tau(\nu; \theta)$ obtained experimentally (upper panel) and by modeling (lower panel). Inset: the modeling results with symmetric inter-flagellar coupling. (F) Effective forcing strength $\varepsilon(\theta)$ as a function of the inter-flagellar coupling asymmetry λ_c/λ_t . Points: measured from simulation; lines: analytical approximation (Eq. (3)); dashed lines: ε_c respectively for the θ_c -flow, θ_a -flow, and θ_t -flow (from top to bottom). (G) Reproducing the flow synchronization of *wt* cells under calcium depletion (H) Reproducing results of *ptx1*. See **Table. 1** for the modeling parameters.

Supplementary materials for The younger flagellum coordinates the beating in *C. reinhardtii*

Da Wei^{1,3}, Greta Quaranta², Marie-Eve Aubin-Tam¹†, Daniel S.W. Tam²*

¹Department of Bionanoscience, Delft University of Technology,
2628CJ Delft, Netherlands.

²Laboratory for Aero and Hydrodynamics, Delft University of Technology,
2628CD Delft, Netherlands.

³Beijing National Laboratory for Condensed Matter Physics, Institute of Physics,
Chinese Academy of Sciences; Beijing 100190, China.

†Corresponding author. Email: m.e.aubin-tam@tudelft.nl;

*Corresponding author. Email: d.s.w.tam@tudelft.nl.

S1 Extracting coupling strength by fitting phase dynamics

In the work described in the manuscript, the flagellum-flow coupling strength ε in *wt* cells is mainly extracted by the synchronization profile $\tau(\nu) \geq 50\%$. Meanwhile, in previous works [1, 2], fitting the distribution of phase dynamics is employed to extract ε . In the latter approach, the idea is that the phase locking during synchronization leads to a peaked probability distribution of $\Delta\varphi$, whose width is affected by the effective noise T_{eff} . The distribution, $P(\Delta\varphi)$, can be derived from the Adler equation **Eq. (1)** as:

$$P(\Delta\varphi) = \int_{\delta_{\text{ct}}}^{\Delta\varphi+2\pi} \exp\left(\frac{V(\Delta\varphi') - V(\Delta\varphi)}{T_{\text{eff}}}\right) d\Delta\varphi'. \quad (\text{S1})$$

Here $V(\Delta\varphi) = \nu\Delta\varphi + \varepsilon \cos(\Delta\varphi)$ is a wash-board potential, T_{eff} is the noise, and $\Delta\varphi$ is the difference between the flagellar phase and the flow's phase.

Here, we demonstrate that these two approaches are equivalent in extracting ε . For all *wt* cells tested in the TRIS-minimal medium (N=11), their $\varepsilon(\theta)$ measured by the $\tau(\nu)$ width and extracted from fitting are plotted against each other, Fig. S1. All points center around the identity line, showing the equivalence in obtaining ε by the two methods. For the *ptxI* dataset, ε are extracted from fitting the phase dynamics.

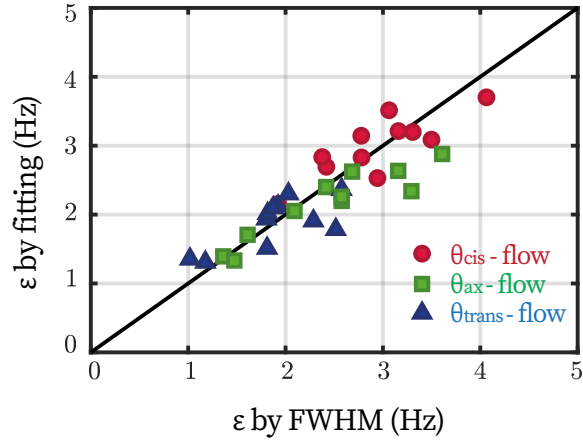


Figure S1: **Equivalence of extracting coupling strength ε by different methods.** Each point represents one cell under either the θ_{a} -flow (green square), the θ_{c} -flow (red circle), or the θ_{t} -flow (blue triangle). The x coordinate is the coupling strength ε measured by the half width of synchronization profile $\tau(\nu) \geq 50\%$; and the y coordinate is obtained by fitting the flagellar phase dynamics.

S2 Hydrodynamic computation for flow along 90 degree

Similar to **Fig. 2** in the main text, we present the computed drag force and power for the flow along 90° . The solid lines and the shadings represent the median and the interquartile range of F_{Flow} and P_{Flow} over the flow-synchronized beats, respectively. Force magnitudes are scaled by $F_0 = 6\pi\mu RU_0 = 9.9$ pN, which is the Stokes drag on a typical free-swimming cell (radius $R = 5$ μm , swim velocity $U_0 = 110$ $\mu\text{m/s}$); while the viscous powers are scaled by $P_0 = F_0 U_0 = 6\pi\mu R U_0^2 = 1.1$ fW. Here $\mu = 0.95$ mPa·s is the dynamic viscosity of water at 22 °C. Quantitatively, the mean force is $0.37F_0$ and $0.34F_0$ (Fig. S2 top panel) while the mean power is $-0.2P_0$ and $-0.4P_0$ (Fig. S2 bottom panel), for the *cis* and the *trans* respectively.

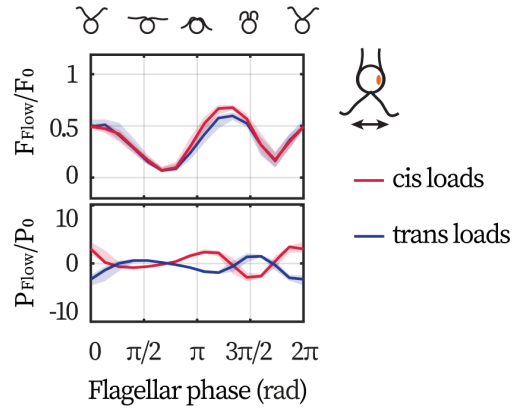


Figure S2: **Computed hydrodynamic loads on the flagella.** Computation results of the drag force (upper panel) and the force's rate of work (lower panel) on the *cis* (red) and the *trans* (blue) flagellum during synchronized cycles, when the cell is subjected to the flow with $\theta = 90^\circ$. Scaling factors $F_0=9.9$ pN and $P_0=1.1$ fW.

S3 The model

The external flow and the two flagella are described by three coupled ordinary differential equations (ODEs). Phase dynamics of these equations are examined by Monte-Carlo simulation. The temporal resolution of simulation (dt) is 1 ms, which corresponds to the experimental frame rates (801 Hz).

$$\begin{cases} \frac{d\varphi_f}{dt} = 2\pi f_f & \text{(S2a)} \\ \frac{d\varphi_c}{dt} = 2\pi f_c - 2\pi\lambda_t \sin(\varphi_c - \varphi_t) - 2\pi\varepsilon_c \sin(\varphi_c - \varphi_f) + \zeta_c(t) & \text{(S2b)} \\ \frac{d\varphi_t}{dt} = 2\pi f_t - 2\pi\lambda_c \sin(\varphi_t - \varphi_c) - 2\pi\varepsilon_t \sin(\varphi_t - \varphi_f) + \zeta_t(t). & \text{(S2c)} \end{cases}$$

The *cis*, the *trans*, and the external flow are described as oscillators, whose intrinsic frequencies are $f_{c,t,f}$ and phases $\varphi_{c,t,f}$, respectively. The flow is assumed to be noise free and the two flagella are assumed to have the same level of noise ($\zeta_c = \zeta_t$). The noises are assumed to be Gaussian, $\langle \zeta_{c,t}(\tau + t) \zeta_{c,t}(\tau) \rangle = 2T_{\text{eff}}^{c,t} \delta(t)$.

S3.1 Flagellar synchronization

Setting ε_c and ε_t to 0, the interaction between the two flagella in the absence of the flow is modeled by:

$$\begin{cases} \frac{d\varphi_t}{dt} = 2\pi f_c - 2\pi\lambda_t \sin(\varphi_c - \varphi_t) + \zeta_c(t) & \text{(S3a)} \\ \frac{d\varphi_c}{dt} = 2\pi f_t - 2\pi\lambda_c \sin(\varphi_t - \varphi_c) + \zeta_t(t). & \text{(S3b)} \end{cases}$$

When the two flagella are able to beat synchronously, $\frac{d\varphi_c}{dt} = \frac{d\varphi_t}{dt} = f_0$, we can obtain the analytical expression of f_0 by adding up $\lambda_c \times \text{Eq. (S3a)}$ and $\lambda_t \times \text{Eq. (S3b)}$:

$$f_0 = \frac{\lambda_t f_t + \lambda_c f_c}{\lambda_c + \lambda_t}. \quad \text{(S4)}$$

Meanwhile, the steady-state phase difference $\delta_{ct} = \varphi_c - \varphi_t$ is obtained by subtracting Eq. (S3a) from Eq. (S3b):

$$\sin(\delta_{ct}) = \frac{f_c - f_t}{\lambda_c + \lambda_t} = \frac{\nu_{ct}}{\lambda_{tot}}. \quad (S5)$$

It is therefore obvious that the two flagella can only beat at the same frequency ($d\varphi_c/dt = d\varphi_t/dt = f_0$) if $|\nu_{ct}/\lambda_{tot}| \leq 1$.

S3.2 Interaction between three oscillators

Now we put the flow back into the picture. According to experimental observations, the two flagella mostly beat synchronously, we therefore focus on this case and first simplify the equations. By adding up $\lambda_c \times \text{Eq. (S2b)}$ and $\lambda_t \times \text{Eq. (S2c)}$, and substituting $\varphi_{c,t}$ as $\varphi_0 = \varphi_c - \delta_{ct}/2 = \varphi_t + \delta_{ct}/2$, we obtain:

$$\frac{d\varphi_0}{dt} = 2\pi f_0 - 2\pi \frac{\lambda_c \varepsilon_c}{\lambda_c + \lambda_t} \sin\left(\varphi_0 - \varphi_f - \frac{\delta_{ct}}{2}\right) - 2\pi \frac{\lambda_t \varepsilon_t}{\lambda_c + \lambda_t} \sin\left(\varphi_0 - \varphi_f + \frac{\delta_{ct}}{2}\right) + \frac{\lambda_t \zeta_t + \lambda_c \zeta_c}{\lambda_c + \lambda_t}. \quad (S6)$$

Given different choices of coupling constants ($\lambda_{c,t}, \varepsilon_{c,t}$), this equation would generate complex phase dynamics - as we shall see in the following sections. We first limit the discussion to small δ_{ct} - as it is observed in our experiment as well as in [3]. The model's asymptotic behavior at $\delta_{ct} \approx 0$ is:

$$\frac{d\varphi_0}{dt} = 2\pi f_0 - 2\pi \varepsilon \sin(\varphi_0 - \varphi_f) + \zeta_0(t), \quad (S7)$$

where

$$f_0 = \frac{\lambda_t f_t + \lambda_c f_c}{\varepsilon_{tc} + \lambda_t}, \quad \varepsilon = \frac{\lambda_t \varepsilon_t + \lambda_c \varepsilon_c}{\lambda_c + \lambda_t}, \quad \zeta_0 = \frac{\lambda_t \zeta_t + \lambda_c \zeta_c}{\lambda_c + \lambda_t}. \quad (S8)$$

In this strong-coupling limit ($\delta_{ct} \approx 0$, or equivalently, $\lambda_{tot} \gg \nu_{ct}$), the coupled flagella behaves as a single oscillator whose beating frequency f_0 will not be interfered by the external flow. The analytical form well captures the system's behavior, as shown by **Fig. 5F**. Next we explore the model's behaviors when $\lambda_{tot} - \nu_{ct}$ is comparable with ε .

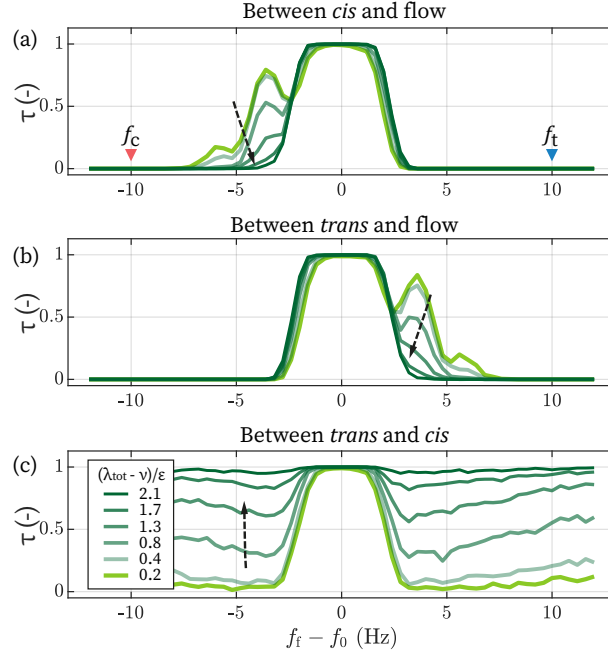


Figure S3: **Determine the lower limit of λ_{tot} .** The time fractions of the *cis* (a) and the *trans* flagellum (b) synchronized by the flow. (c) The time fraction of where *cis* and *trans* are synchronized. Arrows points towards increasing $(\lambda_{\text{tot}} - \nu)/\varepsilon$.

S3.3 Lower limit of inter-flagellar coupling

The value $(\lambda_{\text{tot}} - \nu_{\text{ct}})/\varepsilon$ determines if the flow can disrupt the synchronization between *cis* and *trans*. We assume $\nu_{\text{ct}} = 20$ Hz[4, 5, 6, 3] and focus on synchronization of the θ_a -flow. We plot the synchronization time fractions with increasing λ_{tot} in Fig. S3. When it satisfies $(\lambda_{\text{tot}} - \nu_{\text{ct}})/\varepsilon \geq 2$, external flows cease to affect the flagellar synchronization observably. As the strongest flow ($21U_0$) applied experimentally corresponds to $\varepsilon \approx 10$ Hz, altogether, we conclude that $\lambda_{\text{tot}} \gtrsim \nu_{\text{ct}} + 2\varepsilon_{\text{max}} = 40$ Hz. In the main text, we set $\lambda_{\text{tot}} = 60 = 3\nu_{\text{ct}}$ Hz, which satisfies this relation and matches the observation that the phase lag between the flagella (δ_{ct}) is small.

S4 Flagellar noise of the *ptx1* mutant

Here we show an as-yet uncharacterized strong noise present in the synchronous beating of the mutant *ptx1*. The in-phase (IP) mode of *ptx1* cells and the breaststroke beating of the *wt* cells are similar in waveform and frequency [7, 8]. However, the former has a much stronger noise.

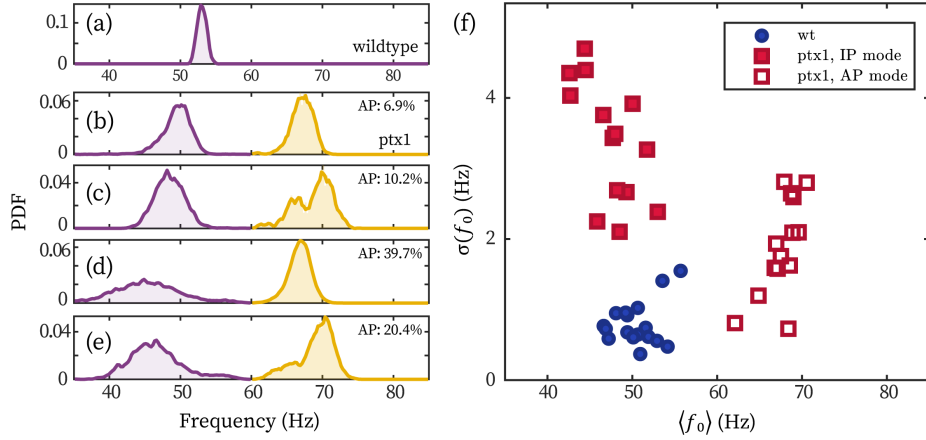


Figure S4: **Stronger frequency fluctuation of the IP mode of *ptx1* cells.** (a-e) Representative probability distributions of the beating frequency of a *wt* (a) and four *ptx1* cells (b-e) over 30 seconds. Probability distributions of the IP (purple) and AP mode (yellow) are respectively normalized for better visualization. The time fractions of the AP mode are noted in each panel. (f) The *wt* and *ptx1* cells represented by its mean beating frequency $\langle f_0 \rangle$ and the standard deviation of the beating frequencies over time $\sigma(f_0)$.

The strong noises show obviously in fluctuations of IP beating frequencies [8].

In Fig. S4, we display the distribution of beating frequency of a representative *wt* cell (panel a) and four representative *ptx1* cells (panels b-e). The broad peaks of the IP (purple) and AP (yellow) beating of *ptx1* sharply contrast the narrow peak of *wt*. We quantify the frequency fluctuations of all the cells in the main text (N=11 for *wt* and N=14 for *ptx1*), Fig. S4f. The cells are represented by its mean beating frequency over time $\langle f_0 \rangle$ and the frequency's standard deviation $\sigma(f_0)$. Clearly, the breaststroke beating of *wt*, the IP, and the AP mode of *ptx1* each forms a cluster. The *wt* cluster is at $(\langle f_0 \rangle, \sigma(f_0)) = (50.5 \pm 2.6, 0.8 \pm 0.3)$ Hz (mean \pm 1 std. the over cell population); and it is evidently less dispersed than both the IP and the AP mode

of *ptx1*, which are at $(47.4 \pm 3.1, 3.4 \pm 0.9)$ Hz and $(67.6 \pm 2.1, 1.9 \pm 0.7)$ Hz, respectively. Under the assumption of a white (Gaussian) noise, $\sigma(f_0)$ is proportional to the noise level ζ , and thus scales with $\sqrt{T_{\text{eff}}}$. Consider that $\sigma(f_0)$ for *ptx1* is 3-5 folds larger than that of *wt*, we therefore conclude that the noise level in *ptx1* is an order of magnitude larger than *wt*, $T_{\text{eff}}^{\text{ptx1}}/T_{\text{eff}}^{\text{wt}} \sim \mathcal{O}(10)$.

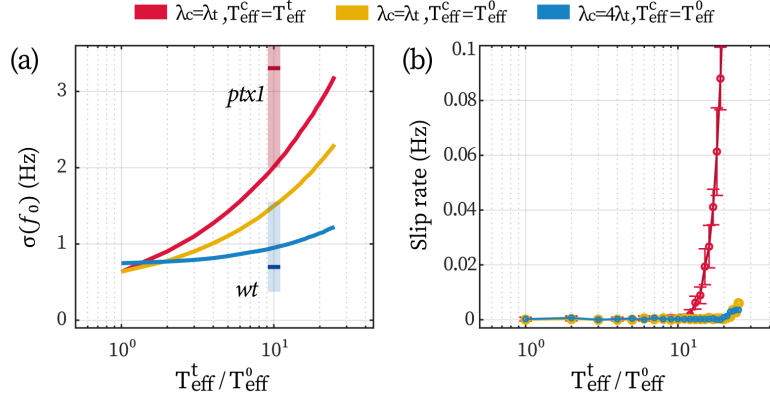


Figure S5: **Effect of a low-noise *cis* in stabilizing the beating of the *trans*** (a) Fluctuations in beating frequency ($\sigma(f_0)$) under different coupling schemes and flagellar noises. Other model parameters are the same as used in the main text. The red and blue shaded area represent the experimentally observed range for *ptx1* and *wt* cells, respectively, with short bars marking the mean values. (b) the rate of slip under the conditions. Error bars correspond to 1 std. over N=9 repetitions.

The stronger noise in *ptx1* can be attributed to two sources, namely, the loss of a stable *cis* and the loss of the unilateral coupling, Fig.S5. We perform Monte-Carlo simulations of the coupled beating of *cis* and *trans* under three conditions: (1) a stable *cis* ($T_{\text{eff}}^c = T_{\text{eff}}^0 = 1.57 \text{ rad/s}^2$) coupled with the *trans* unilaterally ($\lambda_c = 4\lambda_t$), (2) a stable *cis* coupled with the *trans* bilaterally ($\lambda_c = \lambda_t$), and (3) an equally noisy *cis* ($T_{\text{eff}}^c = T_{\text{eff}}^t$) bilaterally coupled with *trans*, see the blue, yellow, and red data in Fig. S5 respectively. It is obvious that, when the *trans* is coupled to a stable *cis*, varying its noise over an order of magnitude only leads to a $\sim 20\%$ stronger frequency fluctuation (the blue line in Fig.S5(a)). On the contrary, lacking either the unilateral coupling or the low-noised *cis* would increase the fluctuation for 200% (yellow

line) or 300% (red line). Qualitatively, simulation results are in agreement with experimental measurements assuming that $T_{\text{eff}}^t/T_{\text{eff}}^c \sim \mathcal{O}(10)$, see the red and blue shaded areas in Fig. S5(a). Moreover, a low-noise *cis* is already sufficient to prevent slips from interrupting the synchrony between *cis* and *trans*, even for bilateral coupling. In Fig. S5(b), as long as the *cis*-noise remains low, slips will be sparse (< 0.01 Hz). Together, these simulation results highlight the stabilizing effect of a low-noise *cis* flagellum, and illustrates the contribution of unilateral coupling in further enhancing the stabilization.

References

- [1] Polin, M., Tuval, I., Drescher, K., Gollub, J. P. & Goldstein, R. E. Chlamydomonas swims with two “gears” in a eukaryotic version of run-and-tumble locomotion. *Science* **325**, 487–490 (2009).
- [2] Quaranta, G., Aubin-Tam, M.-E. & Tam, D. Hydrodynamics versus intracellular coupling in the synchronization of eukaryotic flagella. *Physical Review Letters* **115**, 238101 (2015).
- [3] Wan, K. Y., Leptos, K. C. & Goldstein, R. E. Lag, lock, sync, slip: the many phases of coupled flagella. *Journal of The Royal Society Interface* **11**, 20131160 (2014).
- [4] Kamiya, R. & Hasegawa, E. Intrinsic difference in beat frequency between the two flagella of *Chlamydomonas reinhardtii*. *Experimental Cell Research* **173**, 299–304 (1987).
- [5] Kamiya, R. Analysis of cell vibration for assessing axonemal motility in *Chlamydomonas*. *Methods* **22**, 383–387 (2000).
- [6] Okita, N., Isogai, N., Hirono, M., Kamiya, R. & Yoshimura, K. Phototactic activity in *Chlamydomonas* ‘non-phototactic’ mutants deficient in Ca^{2+} -dependent control of flagellar dominance or in inner-arm dynein. *Journal of Cell Science* **118**, 529–537 (2005).

- [7] Horst, J. & Witman, G. B. *Ptx1*, a nonphototactic mutant of *Chlamydomonas*, lacks control of flagellar dominance. *The Journal of Cell Biology* **120**, 733–741 (1993).
- [8] Leptos, K. C. *et al.* Antiphase synchronization in a flagellar-dominance mutant of *Chlamydomonas*. *Physical Review Letters* **111**, 1–5 (2013).